THE ASTROPHYSICAL JOURNAL, 456:840–849, 1996 January 10

STRUCTURE AND DYNAMICS OF MAGNETIC RECONNECTION IN A SOLAR FLARE

SAKU TSUNETA
Institute of Astronomy, University of Tokyo, Mitaka, Tokyo 181
Received 1995 April 6; accepted 1995 July 14

ABSTRACT

We report a detailed analysis of the temperature structure of a prototypical flare that occurred on 1992 February 21. In the decay phase of this flare, the outer loops systematically have higher temperatures, reaching the peak (12 MK) far outside the apparent bright X-ray loop where the X-ray intensity is only 2%–5% of the peak. In between the high-temperature ridges, a distinct vertical channel with temperature as low as 8–10 MK is seen at the loop top. In the model presented here, these high-temperature ridges are heated by standing isothermal slow shocks attached to a reconnection point higher in the corona. The cool channel would be formed by conduction cooling as the hot reconnection outflow (12–13 MK) traverses with Mach speed ~ 1 (800 km s^{-1}) from the slow-shock region to the loop top. The reconnection point is located 8–18 $\times 10^4$ km above the apparent top of the flare loop (6×10^4 km), and the inflow speed is estimated to be ~ 56 km s^{-1} (Alfvén Mach number ~ 0.07). The bright soft X-ray loops are the reconnected flux tubes subsequently filled with evaporated plasma.

Subject headings: MHD — Sun: flares — Sun: magnetic fields — Sun: X-rays, gamma rays

1. INTRODUCTION

Yohkoh observations (e.g., Tsuneta et al. 1992) unambiguously show that magnetic reconnection at a neutral sheet located at the loop top is responsible for the energy release of at least some flares. An expansion and restructuring of the large-scale active-region fields is sometimes observed prior to the flares and/or in the initial phases of the flares. Tsuneta (1993) suggests that this observed global instability of the active-region magnetic fields creates the neutral sheet, and the subsequent magnetic reconnection plays a key physical role for the flare energy release. (See Pneuman 1981 for the review of the pre-*Yohkoh* observations and the theories, together with Carmichael 1964, Sturrock 1966, Hirayama 1974, Koop & Pneuman 1976.)

The long-duration event (LDE) flare that occurred on 1992 February 21 is particularly suited to the detailed study on magnetic reconnection in solar flares. Except for the peak phase, it was well covered by *Yohkoh* soft X-ray telescope (SXT) observations, and the flare occurred on the limb, allowing us to study the vertical structure. The height and the footpoint separation of the flare loop reach 4–6 $\times 10^4$ km, and the spatial scale involved is far larger than the telescope's spatial resolution, permitting us to study the detailed internal structure of the flare loop.

Tsuneta et al. (1992) reported the initial analysis of the flare and concluded that magnetic reconnection occurs around the top of the flare loop based upon the following evidence: (1) The height and the footpoint separation of the soft X-ray loop increase as a function of time. The rise speed of the inner loop top and the speed of the footpoint separation are ~ 10 km s^{-1}, while that of the outer loop is ~ 30 km s^{-1}. This would be due to the rise of the X-point location along the neutral sheet as reconnection goes on. The apparent height of the reconnected loops (flare loops) and the separation of the footpoints increase with the increasing height of the X-type or inverse Y-shaped reconnection point. (2) The loop-top region has a cusplike structure, implying the location of a reconnection site at the top of the flare loop. It would be hard to create a sharp cusplike structure at the loop top without invoking the singular X-point structure. (3) The outer loops have higher temperatures in the decay phase. This is consistent with a flare energy supplied from the reconnection process near the top of the loop. The outer loops just reconnected are hot, whereas the inner loops are in a cooling process without further major energy input. The *Yohkoh* observations essentially support the classical reconnection model for a "two-ribbon" flare cited above.

Among those pieces of evidence to support magnetic reconnection as the flare energy source, the temperature structure gives key quantitative information to study the structure of the reconnection site. Temperature analysis for this flare, however, has previously been done only for the bright loop (Tsuneta et al. 1992). This paper presents the temperature distribution of the entire active region, including the flare loop, and then discusses the structure and dynamics of the reconnection region.

2. TEMPERATURE STRUCTURE

Figure 1 shows the X-ray time profile of the flare observed by the hard X-ray telescope (HXT) and the soft X-ray spectrometer (SXS) aboard *Yohkoh*. The flare has a soft spectrum in hard X-rays and has a smooth time profile without any impulsive component. (Two small spikes seen in the decay phase occurred in different active regions.)

In the temperature analysis, we sum 20–40 SXT images over 3–21 minutes in time to obtain a better signal-to-noise ratio for high-quality temperature maps for the dim area outside the flare loops. This is possible because the time evolution of the flare is slow: the *e*-folding rise and decay time in the *GOES* 0.5–4 Å channel are 6 minutes (rise) and 100 minutes (decay).

The summation was done after correcting the pointing update of the SXT partial frame location and the spacecraft jitter. Dark-current subtraction was done using a dark image taken at a nearby time. The X-ray filters used in the analysis are the thick aluminum and beryllium filters. The filter combination is suited to temperature analysis for flare plasmas. Figure 2 (Plate 26) shows the temperature, emission measure, pressure, and the soft X-ray maps. The flare occurred on the east limb (N09, E88).

PLATE 26

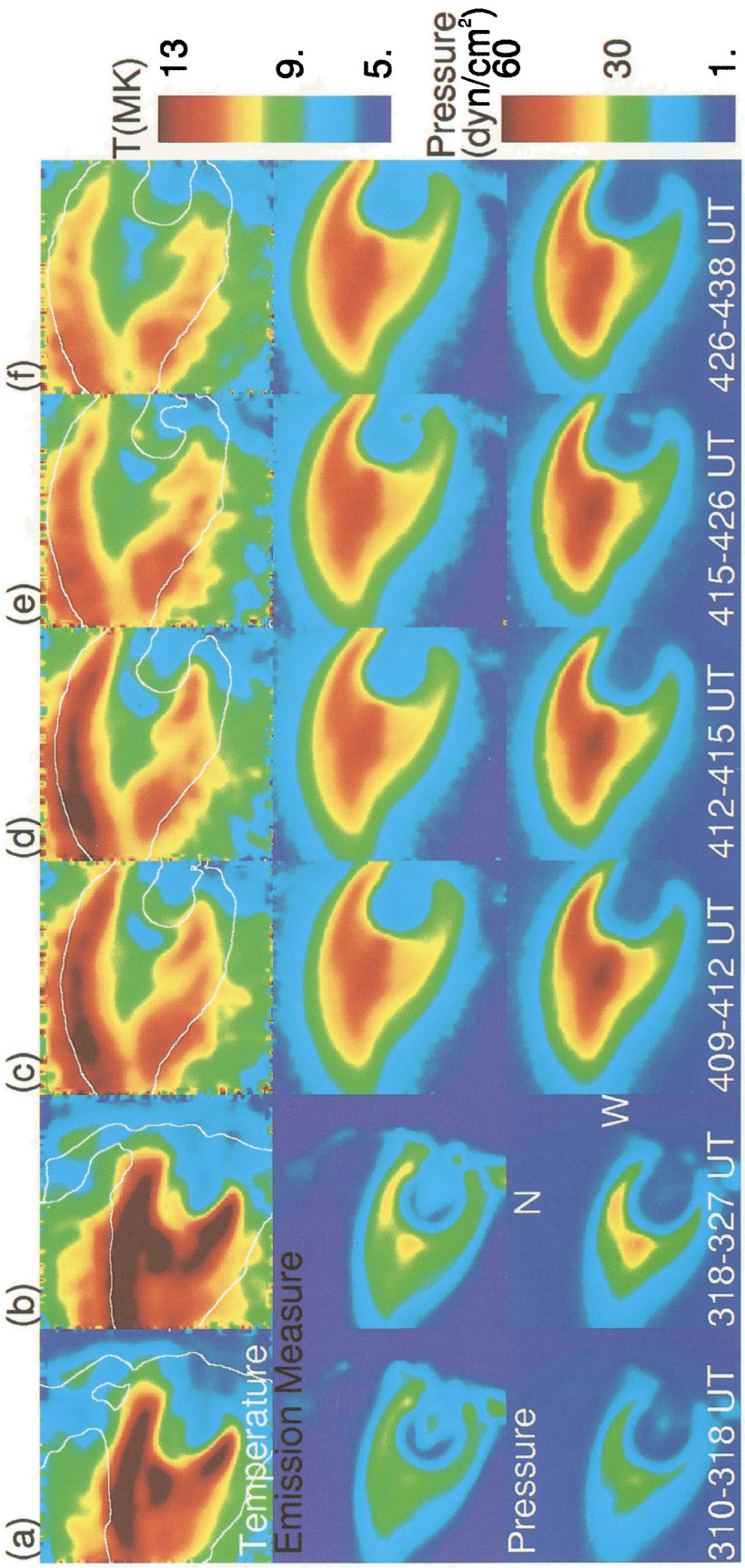

FIG. 2.—Temperature, emission measure, and pressure maps. *From top to bottom:* (*a*) 3:10–3:18 UT, (*b*) 3:18–3:27 UT, (*c*) 4:09–4:12 UT, (*d*) 4:12–4:15 UT, (*e*) 4:15–4:26 UT, and (*f*) 4:26–4:38 UT. The flare occurred on the east limb (N09, E88). North is up, and east is to the left. The FOV is 2′.6, and the pixel size is 2″.46. The location of the FOV changes in between (*b*) and (*c*), and (*a*)–(*b*) and (*c*)–(*e*) are aligned separately. The contours in the top panel indicate 5% level of the peak emission measure in each map.

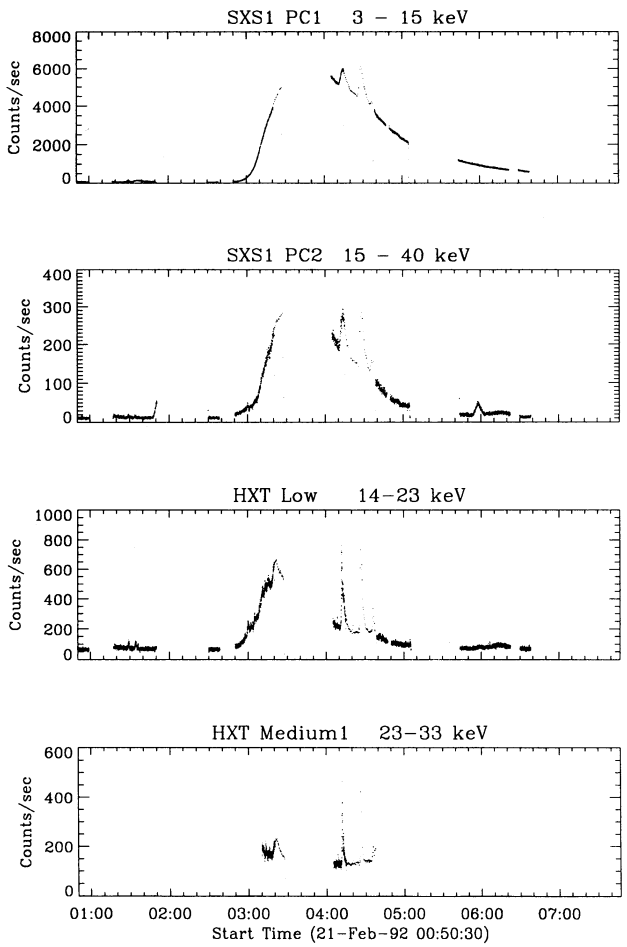

FIG. 1.—X-ray time profile of 1992 February 21 flare. Time profiles are taken with the SXS and the HXT aboard *Yohkoh*. *From top*: SXS channel 1 (3–15 keV), SXS channel 2 (15–40 keV), total counts of HXT subcollimators in the low channel (14–23 keV), and medium 1 channel (23–33 keV). The two small spikes seen in the decay phase come from different active regions.

2.1. *Rise Phase*

Figures 2*a* and 2*b* show that the flare loop has a complex temperature structure in the rise phase. There are three high-temperature regions: long north ridge, south leg, and loop-top compact region. The temperatures in these regions reach 15 MK, higher than the temperatures observed in the decay phase. Among these high-temperature regions, the north ridge appears to evolve into one of the significant temperature ridges seen in the decay phase. The pressure appears to be the highest at the lower loop-top region, reaching 15 dyn cm^{-2}. To estimate pressure, it is necessary to assume a line-of-sight depth, which we take to be a constant 5×10^4 km throughout this paper.

2.2. *Long Decay Phase*

There was no observation near the peak of the hard X-rays, and the *Yohkoh* observations resumed at 4:09 UT, just after the peak of the hard X-rays. The temperature maps for 4:09–4:38 UT (Figs. 2*c*–2*f*) are quite different from those in the rising phase. Figure 3 (Plate 27) shows an enlarged temperature map with emission measure and pressure maps (4:16–4:38 UT). We see two high-temperature ridges where the X-ray intensity is 2%–10% of the peak level. The ridges are apparently located outside or at the outer boundary of the bright flare loop. If we go still further outside, the temperature starts to decrease and returns to the temperature of the active region at 5–6 MK (Kano & Tsuneta 1995; Yoshida & Tsuneta 1996) near the edge of the field of view (FOV). This agreement confirms that the temperatures in the flare region are calibrated with the temperature of the active region. The high-temperature ridges are seen from the start of the postmaximum observation (4:09 UT) through the end of the observation (4:38 UT).

In addition to the ridges, there are two other significant structures: a dense core around the top of the loop and the low-temperature channel in between the two high-temperature ridges. The channel has temperatures as low as 8–10 MK. The cool channel is closely sandwiched by the high-temperature ridges. Figure 4 shows the temperatures, plasma densities, plasma pressures, and radiative losses along the vertical line going through the top of the X-ray loop ("vertical cut"), and along the horizontal line ("horizontal cut") across the cool channel (with respect to the solar surface) as indicated in Figure 3. Figure 5 shows three-dimensional displays of the temperature and the emission measure as seen from the loop-top direction and the footpoint direction. The two ridge structures and the valley (cool channel) in between are clearly seen in the temperature displays of Figure 5. The high-temperature ridges reach the footpoint altitude, suggesting that the magnetic fields in the ridges are the reconnected flux tubes.

The two humps in the temperature profile (horizontal cut of Fig. 4) correspond to the two high-temperature ridges seen in Figures 3 and 5. The peak temperatures are 11–13 MK. The humps sandwich the low-temperature region (cool channel), where the temperature decreases down to 9–10 MK. The density along the horizontal cut has a peak (12×10^9 cm^{-3}) at the cool channel, whereas the densities near the ends of the horizontal cut are $\sim 1 \times 10^9$ cm^{-3}. The pressure also has a peak (35 dyn cm^{-2}) in the cool channel. (The line-of-sight depth is assumed to be 5×10^4 km in these estimates.) The density enhancement of the cool channel is clearly seen in the emission measure display seen from the loop-top side in Figure 5. The radiative energy loss also has a peak in the cool channel owing to the low temperature and the high density.

The vertical cut, on the other hand, shows that the temperature gradually decreases from 10 to 6 MK with lower height. The density and the pressure continue to increase down to the height corresponding to the apparent top of the soft X-ray flare loop. This high-density and high-pressure peak corresponds to the dense core around the loop top, consistent with the accumulation of mass from the reconnection outflow. Both the density and the plasma pressure then rapidly decrease at the height of the pixel location ~40–50 in Figure 4. This cutoff need not be considered the real boundary of the high-temperature matter; instead, it could simply be the height at which the low-temperature plasmas invisible to the *Yohkoh* SXT becomes dominant. The temperature response of the telescope with thick aluminum and beryllium filters has a sharp cutoff at around 4–6 MK. The pressure balance could still be maintained by these unseen low-temperature materials. Tables 1 and 2 summarize the parameters obtained from Figure 4.

3. MAGNETIC STRUCTURE AND DYNAMICS OF MAGNETIC RECONNECTION

In this section, we describe the magnetic structure and the dynamics of the reconnection region of the flare from the

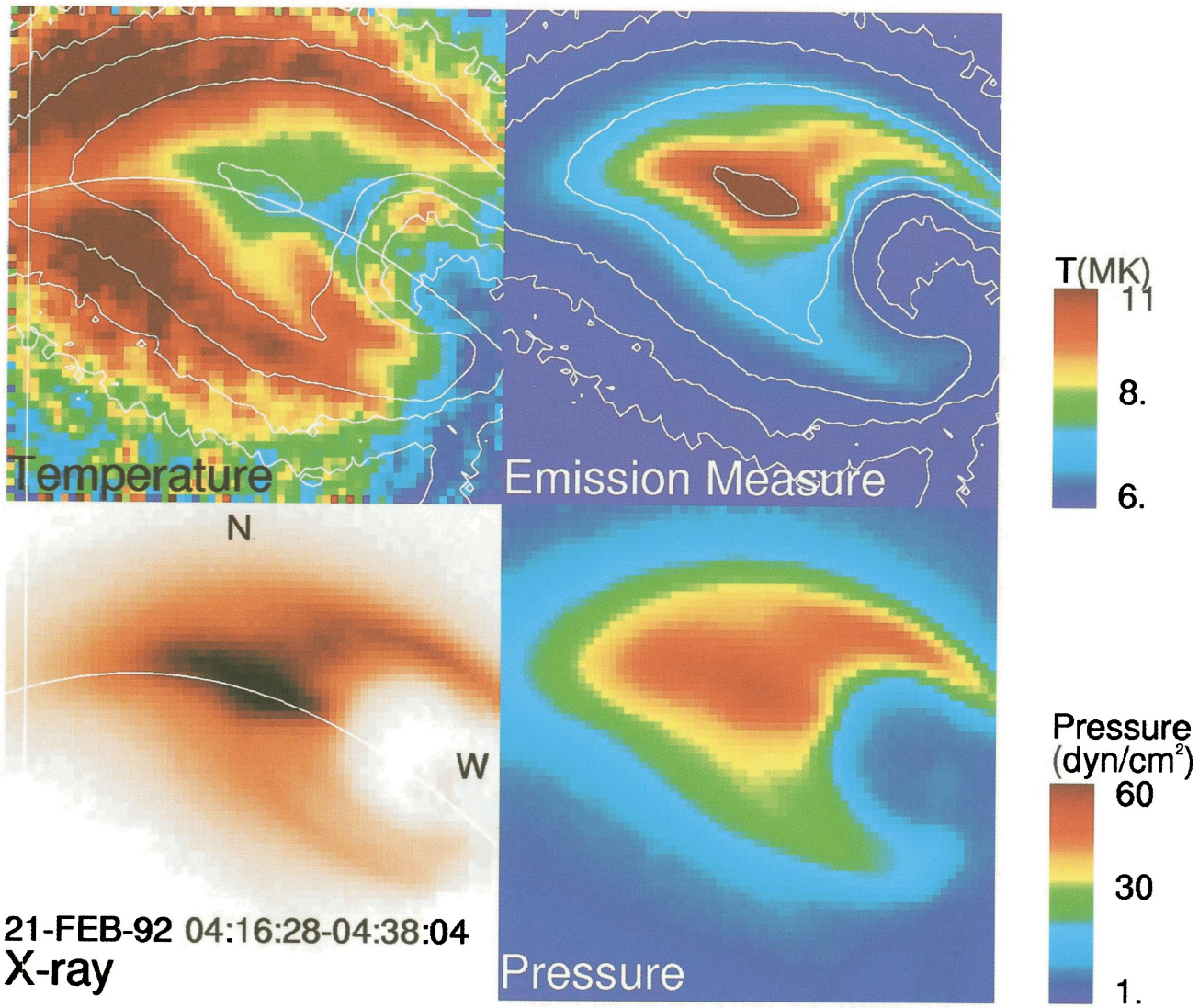

FIG. 3.—Temperature, emission measure, pressure, and X-ray (thick aluminum filter) maps of the 1992 February 21 flare. The flare occurred on the east limb (N09, E88). North is up, and east is to the left. The contours in the temperature and emission measure maps indicate the locations of 83%, 20%, 5%, 2%, and 1% levels of the peak X-ray intensity of the map. The size of the FOV is 2.'6, and the pixel size is 2."46. The data taken from 4:16 to 4:38 UT, early decay phase in soft X-rays, are summed to obtain the high-quality temperature maps for the low-intensity region outside the flare loop.

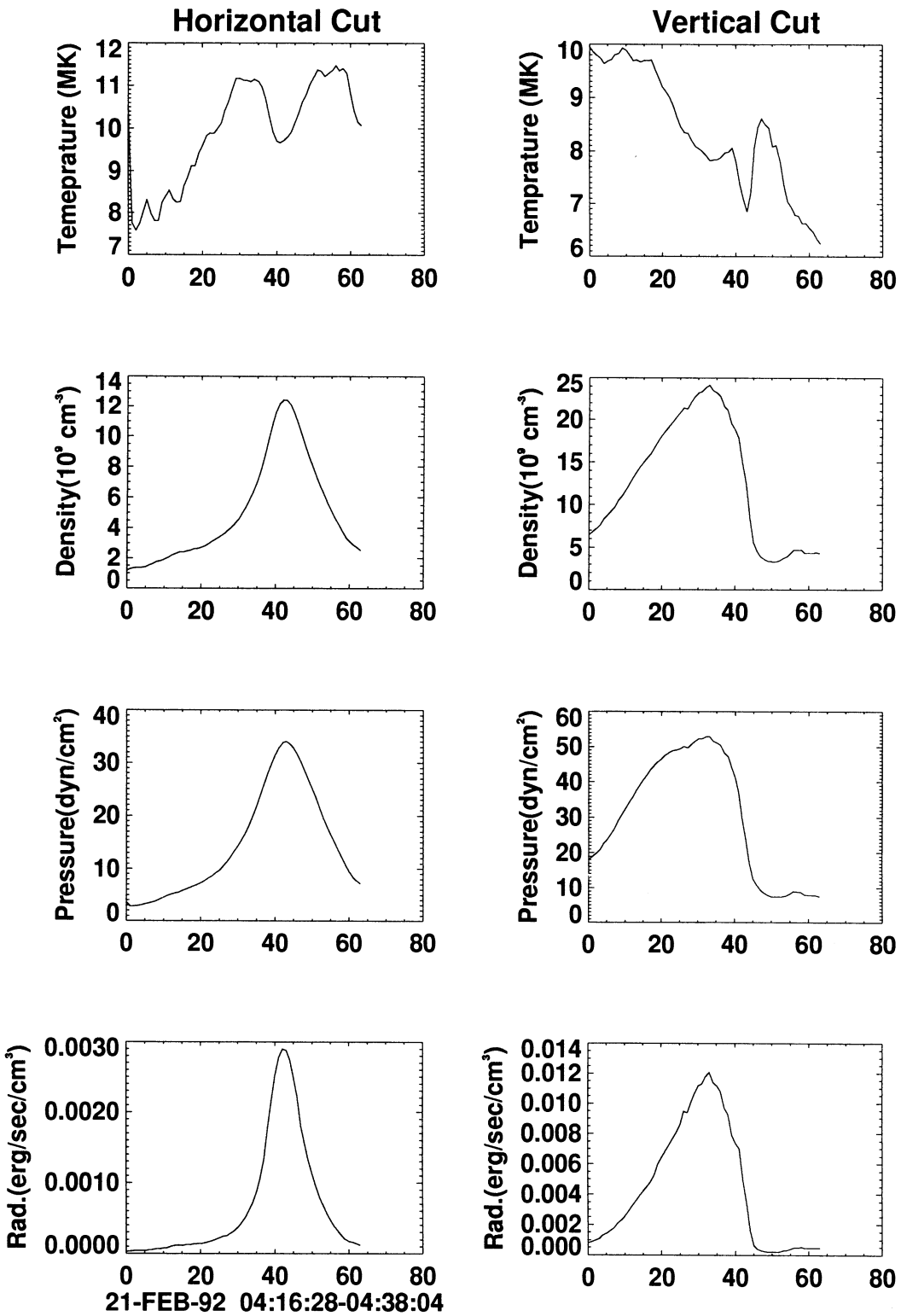

FIG. 4.—Temperature, plasma density, pressure, and radiative loss along the horizontal and vertical (with respect to the solar surface) lines shown in Fig. 3 (4:16–4:38 UT). The abscissa is the pixel number of the CCD along the lines. The size of the CCD pixel is 2.″46 (1780 km). The two humps in temperature horizontal cut correspond to the high-temperature ridges. The low-temperature region in between the high-temperature ridges is the cool channel with sharp increase of the plasma density, pressure, and radiative loss flux. The vertical cut shows decreasing temperature and increasing density and pressure with lower height.

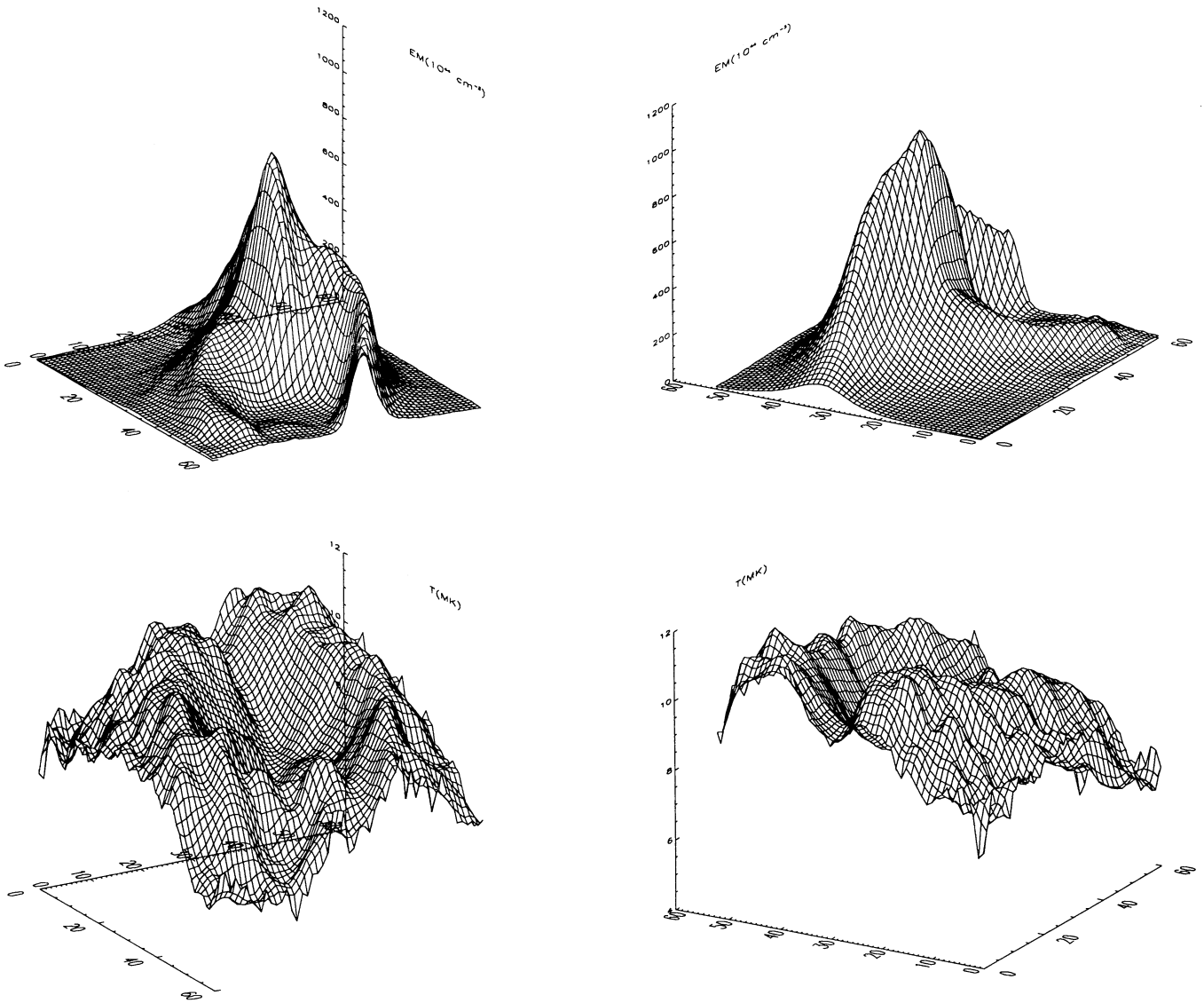

FIG. 5.—Three-dimensional display of the temperature and the emission measure. The data are the same as Fig. 3 (4:16–4:38 UT). *Top left*: emission measure distribution as seen from the footpoint direction. *Top right*: emission measure distribution as seen from the loop-top direction. *Bottom-left*: temperature distribution as seen from the footpoint direction. *Bottom-right*: temperature distribution as seen from the loop-top direction. The ridges and the valley structure of the temperature are clearly seen. The temperature of the ridges decreases with lower height, and the ridges reach the footpoint height. The dense loop structure is located inside the high-temperature ridges.

TABLE 1

PHYSICAL PARAMETERS OF UPSTREAM/DOWNSTREAM OF THE MAGNETIC SEPARATRIX LINES AND SLOW SHOCK

Parameter	Upstream	Downstream
Temperature	<7 MK	>12–13 MK
Density	10^9 cm^{-3}	$<5 \times 10^9$ cm^{-3}
Pressure	3 dyn cm^{-2}	<20 dyn cm^{-2}
Magnetic field	20–30 G	5 G
Plasma β	~ 0.25	~ 30
Flow velocity	56 km s^{-1}	800 km s^{-1}
Sound Mach number	~ 0.1	~ 1
Alfvén Mach number	~ 0.07	~ 5
Alfvén speed	800 km s^{-1}	155 km s^{-1}
Sound speed	550 km s^{-1}	770 km s^{-1}
Mass flux	$\sim 1.7 \times 10^{35}$ s^{-1}	$\sim 2.4 \times 10^{35}$ s^{-1}

Yohkoh observations by employing the theory of Petschek (1964). The compressible nature of the plasma is taken into account when necessary.

3.1. *Overall Magnetic Structure*

Figure 6 shows the magnetic structure inferred from the observations. The reconnection point is located high above the apparent flare loop. The standing slow shocks are attached to the reconnection point (Forbes & Priest 1982, 1983; Cargill & Priest 1983; Ugai 1987, 1989, 1992; Forbes & Malherbe 1991). The X-point and the slow shocks themselves would be located outside the *Yohkoh* field of view. There is an inflow toward the X-point and the slow shocks from the active-region corona. Fast outflows come from the reconnection site both upward and downward.

TABLE 2

PHYSICAL PARAMETERS OF THE RECONNECTION REGION

Parameter	Value
Cool channel temperature	10–6 MK
Cool channel density	5–25 × 10^9 cm^{-3}
Cool channel pressure	20–50 dyn cm^{-2}
Density jump across the slow shock	<5
Temperature jump across the slow shock	~ 1 ($\gamma \sim 1$)
Half-angle of the slow shocks	0°8–1°8
Half-angle of the separatrices	5°–11°
Kinetic energy of the outflow	5 × 10^{27} ergs s^{-1}
Shock heating rate	9 × 10^{27} ergs s^{-1}
Total energy	14 × 10^{27} ergs s^{-1}
Magnetic energy supply from the upstream	6 × 10^{27} ergs s^{-1}
Soft X-ray loop height	$\sim 6 \times 10^4$ km
X-point height	$\sim$14–24 × 10^4 km above the photosphere $\sim$8–18 × 10^4 km above the loop top
Slow shock length	$\sim$a few × 10^4 km

The high-temperature ridges are located along the reconnected field lines that go through the slow shocks. The separatrices which separate the reconnected field lines from the upstream field lines would be located at the outer edge of the high-temperature ridges. From the horizontal cut density profile (Fig. 4), the upstream plasma density and the pressure are thus 1 × 10^9 cm^{-3} and 3 dyn cm^{-3}, respectively. Those in the downstream are 5 × 10^9 cm^{-3} and 20 dyn cm^{-2}, respectively, from the vertical cut profiles. The plasma is then compressible. The densities and pressures closer to the shock region in the downstream would be lower, because the vertical cut profiles show decreasing density and pressure with higher altitude.

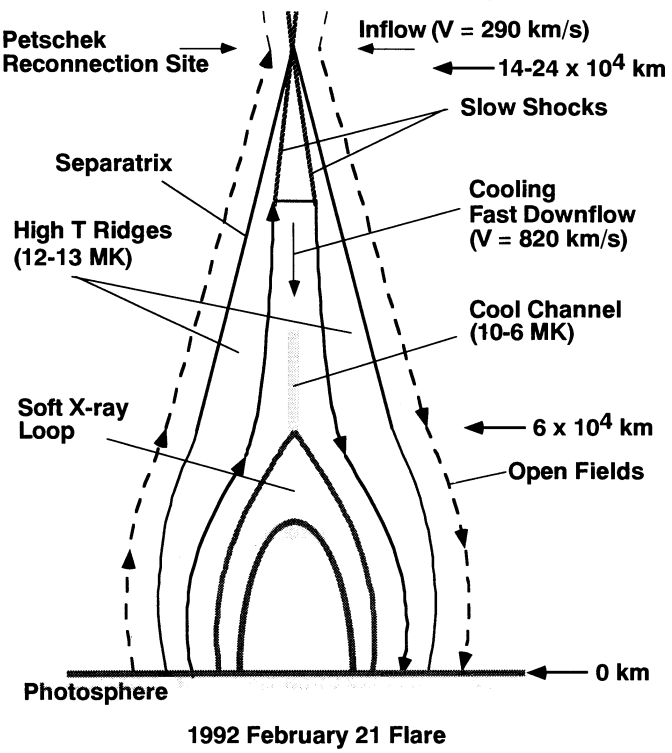

FIG. 6.—Inferred magnetic structure of the reconnection site. The reconnection point is located high above the apparent flare loop. The slow shocks are attached to the reconnection point (diffusion region). There is an inflow toward the X-point and the slow shock from the active-region corona. The fast outflows come from the reconnection site upward and downward. The cool channel located in between the high-temperature ridges is a cooling outflow from the reconnection site.

The plasmas on the reconnected field lines are significantly heated by the two standing slow shocks. This is clearly seen as two high-temperature ridges (11–13 MK) in Figure 3 and as the two humps seen in Figure 4. There should be a fast flow from the reconnection site. The cool channel seen in between the high-temperature ridges would correspond to the cooling fast flow. The initial temperature of the outflow would be similar to or higher than those of the high-temperature ridges (11–13 MK). The flow is then rapidly cooled on its way down by conduction along the field lines, as we will see in the subsequent section. When it enters the *Yohkoh* field of view, its temperature is as low as 10 MK. As it moves further downward, the temperature decreases to 6–7 MK near the top of the soft X-ray loops. This picture naturally explains the existence of both hot and cool plasmas in close proximity, because they are separated by the magnetic fields.

The primary shock heating goes on in the low-density reconnected loops (high-temperature ridges) above the observed flare loops. This dumps a significant amount of energy into the chromosphere via heat conduction, resulting in chromospheric evaporation. The timescale of the plasma filling is of the order of 10 minutes for the speed of evaporated plasmas $\sim$100 km s^{-1} and the loop height of 6 × 10^4 km. This slow filling of the plasma to the reconnected loops explains the X-ray–bright flare loop located below the high-temperature ridges. Indeed, Figure 6 shows the spatial relationship of the high-density loops filled with the evaporated plasmas and the surrounding high-temperature ridges. The high-density flare loops, bright in soft X-rays, are the aftereffects of the energy release by the slow shocks.

The shock heating would also occur for the outflow going upward (away from the Sun) from the reconnection site. This upward plasma has temperatures as high as the observed temperatures of the ridges, because the outflows are symmetric around the X-point. The plasma density of the upward-moving loops does not change much, becuase there is no contribution of chromosphere evaporation. Although this upward flow is located outside the field of view in this flare, it is important to find the upward flow in other events to verify the scenario presented here. Since the velocity of the upward outflow

exceeds the Sun's escape velocity (618 km s^{-1}), as we will see, the outflow may reach the interplanetary space. The high-temperature dense outflow is distinct in the solar wind. The detection may thus be possible with in situ interplanetary observations, although the upward outflow would be beamed with narrow angle.

3.2. *The Cool Channel and the Height of the X-Point*

There is a fast outflow from the reconnection point (diffusion region) located in between the two standing slow shocks. The speed V of the reconnection outflow reaches the Alfvén velocity of the upstream V_A ($\sim$800 km s^{-1} for a magnetic field of 20 G and plasma density of 3×10^9 cm^{-3}), and the temperature of the downstream just outside the slow shocks is close to the observed temperature of the ridges, owing to the good thermal conductivity along the field lines (isothermal shock). The flow would be gradually cooled by conductive energy loss on its way from the reconnection site to the top of the flare loop, forming the observed cool channel. Indeed, the temperature along the vertical cut in Figure 4 shows a gradual decrease with lower altitude.

We can estimate the height of the X-point (reconnection point, diffusion region) from the consideration of the cooling time. The radiative cooling time of the outflow is expressed as

$$t_{\rm rad} = \frac{3nkT}{\Lambda(T)n^2}, \tag{1}$$

where k is the Boltzmann constant and $\Lambda(T)$ is the radiative loss function (Mewe, Gronenschild, & van den Oord 1985; Mewe, Lemen, & van den Oord 1986). Since the density n is 14×10^9 cm^{-3}, the temperature $T \sim 13$ MK, and the radiative loss function $\Lambda(T) = 6 \times 10^{-20}\, T^{-0.5} \sim 1.7 \times 10^{-23}$ ergs s^{-1} cm^{-3} in the cool channel, the radiative cooling time $t_{\rm rad}$ is 1.7×10^4 s. The conduction cooling is given by

$$t_{\rm cond} = \frac{3nkTl}{\kappa_0 T^{5/2}(T/l)}, \tag{2}$$

where $\kappa_0 T^{5/2}$ is the Spitzer thermal conductivity ($\kappa_0 = 10^{-6}$ [ergs s^{-1} cm^{-1} $K^{-3.5}$]), and l is the scale length of the temperature drop along the high-temperature ridges. The conduction timescale $t_{\rm cond}$ is 104–228 s for $l = 4$–6×10^4 km. Although there is a sharp peak of the radiation loss in the cool channel, this is negligible in cooling the hot plasma ejected from the reconnection site. The hot outflow plasma is rapidly cooled down as a result of conduction to the chromosphere along the reconnected field lines. These cooling loops are naturally located below the high-temperature ridges. Since the cooling times of the outflow plasma are 104–228 s, the location of the reconnection point is about 8–18 $\times 10^4$ km ($\sim$800 km s^{-1} $\times$ 104–228 s) above the cool channel, because the hot downflow has to be conductively cooled down until it reaches the cool channel. Since the height of the apparent flare loop is $\sim 6 \times 10^4$ km, the height of the X-point is then about 14–24 $\times 10^4$ km.

Note that all the flares do not necessarily have the cool channel as this flare does. Whether to have the cool channel or not depends on the distance between the X-point (diffusion region) and the top of the loop. If the distance is close, the outflow reaches the loop top without cooling, and there is no distinct cool channel at the loop top.

3.3. *Standing Slow Shocks*

Let us examine the standing slow shocks attached to the X-point. We can assume that the slow shocks are the switch-off shocks (Fig. 6). From the jump condition, we obtain

$$\frac{n_{\rm down}}{n_{\rm up}} \le 1 + \frac{1}{\gamma(\beta_{\rm up} + 1) - 1} \sim 1 + \frac{1}{\beta_{\rm up}}, \tag{3}$$

where $n_{\rm down}$ is the plasma density in the downstream of the slow shock, $n_{\rm up}$ the plasma density in the upstream, $\beta_{\rm up}$ the plasma beta in the upstream, and γ the specific heat ratio. (The equality in eq. [3] holds, when the upstream magnetic field lines are parallel to the shock.) We assume isothermal shocks due to high thermal conductivity along the field lines; $\gamma \sim 1$. The density in the upstream flow can be directly obtained from the horizontal cut profiles of Figure 4; $n_{\rm up} \sim 1 \times 10^9$ cm^{-3}. The density in the downstream flow is similar to the density in the cool channel; $n_{\rm down} < 5 \times 10^9$ cm^{-3}. The ratio is thus $\sim$4–5, and $\beta_{\rm up}$ is therefore smaller than 0.25. The plasma $\beta_{\rm up}$ does not depend on the assumed line-of-sight length of the region. Since the plasma pressure in the upstream is $\sim$5–10 dyn cm^{-2} from the horizontal cut of Figure 4, the magnetic field strength in the upstream flow $B_{\rm up}$ is $\sim$20–30 G. The Alfvén speed in the upstream, V_A, is 800 km s^{-1} for $B \sim 20$ G and $n \sim 3 \times 10^9$ cm^{-3}. The outflow speed is then $V \sim V_A \sim$ 800 km s^{-1}.

Since the magnetic field strength in the downstream flow $B_{\rm down}$ is $\sim$5 G (see § 3.5), the Alfvén velocity $V_{A\,\rm down}$ in the downstream flow is $\sim$155 km s^{-1} ($n = 5 \times 10^9$ cm^{-3}). The sound velocity C_s in the downstream flow is $\sim$770 km s^{-1} ($p = 30$ dyn cm^{-2}, $n = 5 \times 10^9$ cm^{-3}). Thus, we obtain the downstream Mach number $M_{\rm down} = V/C_s$ to be $\sim$1. The downstream plasma beta, $\beta_{\rm down} \sim 6C_s^2/4V_{A\,\rm down}^2$, is $\sim$30.

3.4. *Absence of Fast (Perpendicular) Shock*

We obtain $V \sim C_s \gg V_{A\,\rm down}$ from the estimation of the previous section, where V is the velocity of the outflow and C_s and $V_{A\,\rm down}$ are the sound and Alfvén speeds in the outflow. The condition to have a fast (perpendicular) shock is

$$V^2 > C_s^2 + V_{A\,\rm down}^2 \tag{4}$$

(Priest 1982). If a perpendicular shock is formed, the jump condition predicts that

$$\frac{n_2}{n_1} = \frac{B_2}{B_1} = \frac{(\gamma + 1)M_1^2}{2 + (\gamma - 1)M_1^2}, \tag{5}$$

where the subscripts 1 and 2 denote the upstream and downstream values of the fast shock. To obtain equation (5), we have assumed plasma $\beta_1 (\equiv \beta_{\rm down}) \gg 1$, as we have seen in the previous section. The equation is reduced to the hydrodynamic one (Priest 1982).

Since $(C_s^2 + V_{A\,\rm down}^2)^{0.5} \sim 785$ km s^{-1}, if we consider the errors of these estimates, it is marginal whether the condition for the fast shock holds near the loop top or not. The outflow velocity V weakly depends on the assumed line-of-sight thickness d ($V \propto d^{1/4}$), and the sound velocity C_s does not depend on d. If $M_1 (\equiv M_{\rm down} = V/C_s)$ is close to unity, the shock is weak from equation (5). As long as the Mach number exceeds $\sim$1 in his numerical simulations, Ugai (1987) observes the transient formation of a fast shock around the colliding point of the fast outflow from the reconnection site with the closed-loop structure (see also Forbes & Priest 1983; Forbes & Mal-

herbe 1991). However, this is probably not the case for this particular flare.

The compact high-temperature source at the loop top seen in the rise phase (Figs. 2*a* and 2*b*) may be the result of the perpendicular shock. This, however, disappears in the decay phase, where we only see the low-temperature (6–8 MK) dense (3×10^{10} cm^{-3}) core near the loop top. In the initial phase, the speed of the reconnection outflow could be faster than that in the decay phase owing to the lower altitude of the reconnection point (i.e., stronger magnetic fields) and may satisfy the condition for a fast shock, resulting in the formation of the high-temperature region at the loop top in the early phase.

Masuda et al. (1994) discovered a compact impulsive hard X-ray source just *above* the soft X-ray flare loop, in addition to the usual double footpoint hard X-ray sources for several impulsive flares. These impulsive flares are more compact in size than the flare discussed in this paper, implying stronger magnetic fields. This results in faster outflow. Thus, it is easier to have fast-shock heating near the loop top as compared with the larger LDE flare with weaker magnetic fields. The hard X-ray source above the loop top may thus be a signature of the perpendicular shock heating.

3.5. *Reconnection Inflow and Outflow*

In this section, we obtain the inflow speed of the upstream plasma. From the conservation of the mass flux across the shock, the upstream flow speed V is expressed as

$$V = V_A \tan \alpha \frac{n_{down}}{n_{up}}, \quad (6)$$

where V_A is the Alfvén velocity in the upstream and α is the acute half-angle of the slow shocks. The acute half-angle of the separatrices β is also given by

$$\tan \beta = \left(1 + \frac{n_{down}}{n_{up}}\right) \tan \alpha . \quad (7)$$

(The compressible nature of the slow shocks is taken into account in eqs. [6] and [7].) Since $n_{down}/n_{up} \sim 5$, we have $\beta \sim 6\alpha$. Thus, we can estimate the inflow speed from the observed mutual angle of the separatrices. The separatrices of reconnection would be located at the outer edge of the high-temperature ridges. The angle of the separatrices can be estimated from the estimated height of the X-point (diffusion region) and the observed distance of the two high-temperature ridges. The separation of the outer boundaries of the north and the south high-temperature ridges at the loop top is $\sim 3 \times 10^4$ km, and the height of the X-point from the top is about $8–18 \times 10^4$ km, as estimated in the previous section. From these two values, we estimate the half-angle of the separatrices β to be 5°–11°, assuming the semitriangular shape of the separatrices as shown in Figure 6. The acute half-angle of the slow shocks $\alpha \sim \beta/6$ is then 0°.8–1°.8. The inflow velocity is then 56 km s^{-1} for the slow-shock angle α of 1°, $n_{down}/n_{up} \sim 4$, and $V_A \sim 800$ km s^{-1}. The Alfvén Mach number of the upstream flow is 0.07. Since the inflow speed is high, there is a possibility that reconnection goes on intermittently.

The magnetic field strength in the downstream B_{down} is $B_{up} \sin(\beta - \alpha)/\cos \alpha$ from the conservation of the normal component of the magnetic flux. If we take $\alpha \sim 1°$ and $\beta \sim 11°$, the magnetic field strength in the downstream is $B_{down} \sim 5$ G.

Since the width of the high-temperature ridges is $\sim 1 \times 10^4$ km, the shocks would have longer macroscopic length (Fig. 6). The length is far larger than the size of the diffusion region, which would be extremely small in size due to the high electrical conductivity. This suggests a picture of macroscopic slow shocks attached to a pointlike X-point (diffusion region). The overall magnetic structure of the reconnection region must be remarkably simple (as shown in Fig. 6).

The inflow particle flux N_{up} brought with the inflow magnetic flux is expressed as

$$N_{up} = n_{up} V S , \quad (8)$$

where V is the upstream velocity, n_{up} the plasma density in the upstream, and S the cross-sectional area of the inflow region. If we adopt $V \sim 56$ km s^{-1}, $n_{up} \sim 1 \times 10^9$ cm^{-3}, $S \sim 5 \times 10^4$ km (along the line of sight) $\times 6 \times 10^4$ km (vertical length), the total number of ions brought with the inflow is estimated to be 1.7×10^{35} s^{-1}. This should match with the outflow flux. The outflow flux is estimated to be

$$N_{down} = n_{down} V_A s , \quad (9)$$

where V_A is the downstream velocity, n_{down} the plasma density in the downstream, and s is the cross-sectional area of the outflow. We take $n_{down} \sim 3 \times 10^9$ cm^{-3}, $V_A \sim 800$ km s^{-1}, and assume s to be 5×10^4 (along the line of sight) $\times 2 \times 10^3$ km (horizontal length of the outflow). The total number of ions in the outflow is then 2.4×10^{35} s^{-1}.

The plasma density and the pressure of the soft X-ray loop top increase as a function of time. The pressure also increases with decreasing height along the cool channel. This indicates the accumulation of the mass from the reconnection site at the loop top. The high-pressure region at the loop top would be maintained and confined against gravity by concave ("U-shaped") magnetic fields. The convex magnetic fields at the loop top become concave by the fast outflow. This is clearly seen in the numerical simulation of Forbes & Malherbe (1991). The horizontal (loop) magnetic fields located below the apparent flare loop balance the plasma pressure: the field strength below the apparent flare loop is $B \sim (8\pi p)^{0.5} \sim 40$ G ($p \sim 60$ dyn cm^{-2}), where p is plasma pressure of the loop-top region.

The total amount of plasma at the loop top in the rise phase is 2×10^{38} particles ($n \sim 2 \times 10^{10}$ cm^{-3} and the volume is $\sim 10^{28}$ cm^3). This plasma cannot be supplied by chromospheric evaporation (plasma filling from below) because the pressure of the loop top is higher than that of the footpoints by about a factor of 2–3. The plasma must be supplied by the reconnection outflow. The reconnection outflow can supply the mass for the loop-top dense regions with timescale of ~ 14 minute ($\sim 2 \times 10^{38}/2.4 \times 10^{35}$ s^{-1}). Nevertheless, chromospheric evaporation plays dominant part in filling the reconnected flux tubes. The peak number of particles in the reconnected loops is $\sim 10^{29}$ cm$^3 \times (2 \times 10^{11}$ cm$^{-3}) \sim 2 \times 10^{40}$, which is much larger than the total number of outflow particles from the reconnection site.

We assume that the line-of-sight length is constant in the above discussion. If the line-of-sight thickness of the loop top is larger than that of the footpoints by a factor of 4–9, pressure may be almost uniform along the loop. Then, chromospheric evaporation may also contribute to the loop filling near the loop top.

3.6. *Rarefaction of Upstream Corona*

The large inflow flux implies that the upstream corona can be rarefied as a result of reconnection. We thus examine the time evolution of the X-ray intensity of the upstream corona.

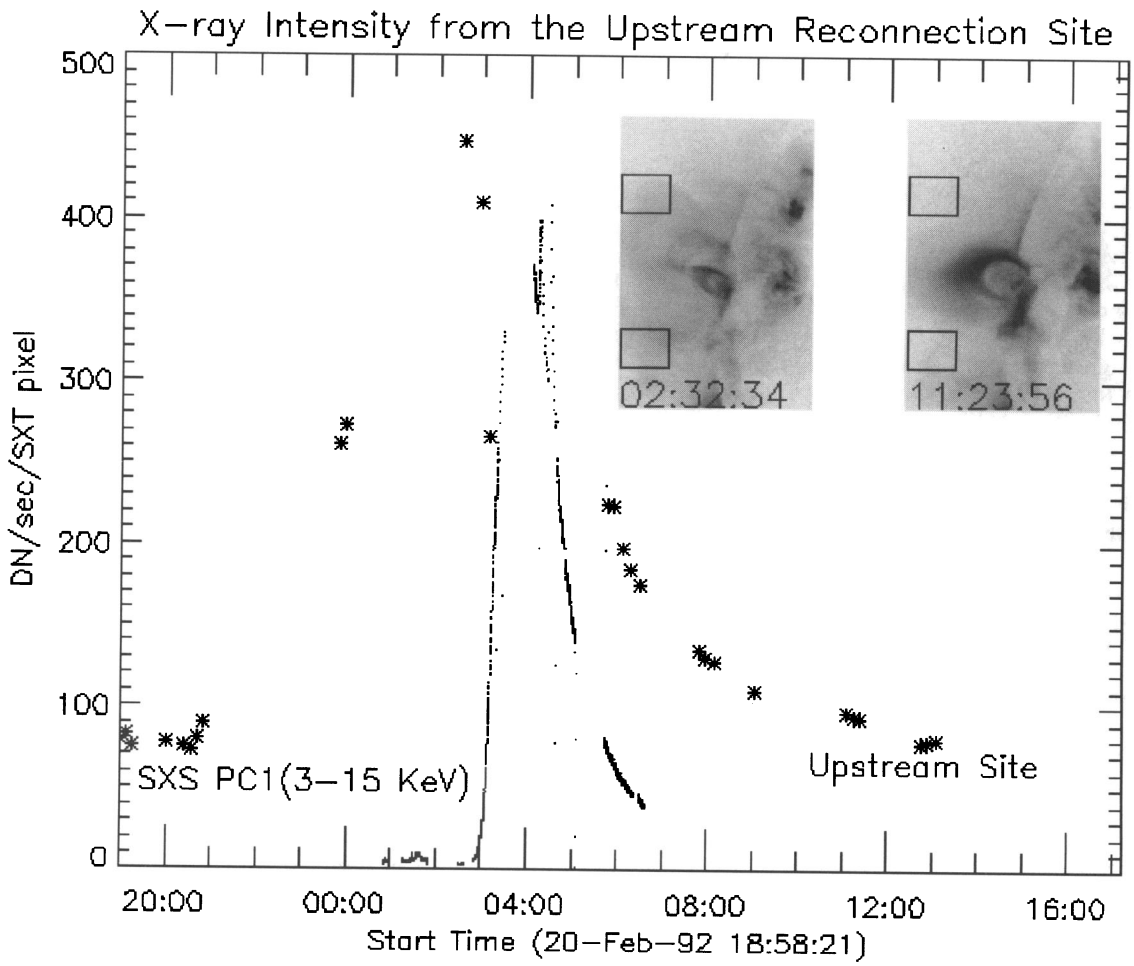

FIG. 7.—Time evolution of the soft X-ray intensity of the upstream corona (*asterisks*) from 8 hr before the flare through 10 hr after the flare. The location of the upstream corona is marked by the boxes in the inserted X-ray images. The boxes are located on both sides of the neutral sheet. The scattered photons from the bright flare loop are subtracted. The soft X-ray time profile, as observed with the SXS (3–15 keV), is also shown. There is a gradual increase in the coronal emission before the flare, followed by the rapid decrease at the start of the flare. In the decay phase, there is a gradual decrease of the coronal emission, followed by the decrease of the X-rays from the flare loop. This suggests the rarefaction of the upstream corona due to the fast magnetic reconnection at the neutral point above the flare loop.

Figure 7 plots the X-ray intensity from the upstream corona located on both sides of the neutral sheet (marked by the boxes in the inserted X-ray images of Fig. 7). We estimate the effect of the scattered photons from the bright flare loop to the dark upstream regions. The scattering is the result of the micro-roughness of the grazing-incidence X-ray mirror and is represented by the power-law wing of the point-spread function. Hara et al. (1994) obtained the analytic form of the wing component using the in-flight flare data. We estimate the number of the scattered photons from bright regions with the wing component of the point-spread function given by Hara et al. (1994). We find that the scattered photons to the dark region are 8%–21% of the intensity of the dark region. The contribution from the scattered photons is subtracted in Figure 7. Figure 7 also shows the time profile of the flare obtained with the SXS aboard *Yohkoh*.

There is a gradual increase in the active-region coronal emission over 6–7 hr prior to the flare. This is followed by the sharp decrease (about a factor of 2) in the coronal emission at the onset of the flare just when the soft X-rays rapidly increase. This may be the result of the expansion of the active-region fields prior to the flare (Tsuneta et al. 1992). In the decay phase, there is a gradual decrease of the coronal emission, following the decrease of the X-rays from the flare loop. The coronal emission returns to the preflare value about 10 hr after the flare. The net decrease of the emission is a factor of ~2–5. We assume that the decrease in the coronal intensity is due to a change in the emission measure, since the temperature of the active region would be constant. Since the change of the emission measure is a factor of 2–5, the density decrease $\delta n_{\rm up}$ is 0.6–1.1 $\times$ 10^9 cm^{-3} for $n_{\rm up} \sim 2 \times 10^9$ cm^{-3}. This decrease in density may correspond to the mass flux brought to the reconnection region. The fast inflow and the observed rarefaction of the upstream corona appear to be consistent.

3.7. *Energy Balance*

The kinetic energy flux of the outflow is estimated to be

$$E_{\rm flow} = \frac{m_p}{2}\,(n_{\rm down}\, sV_{\rm A})V_{\rm A}^2 + \frac{3}{2}\,p_{\rm down}\, sV_{\rm A}\,, \qquad (10)$$

where s is the cross-sectional area of the outflow, $p_{\rm down}$ is the plasma pressure of the outflow, and m_p is the proton rest mass. The first term in equation (10) is the energy flux of the bulk

outflow, and the second term is the thermal energy carried by the outflow. If we take $n_{down} \sim 4 \times 10^9$ cm^{-3}, $s \sim 10^{18}$ cm^2 (width of the cool channel [2×10^3 km] $\times$ assumed line-of-sight thickness [5×10^4 km]), $p \sim 30$ dyn cm^{-2}, and $V_A \sim 800$ km s^{-1}, we obtain $E_{flow} \sim 1.7 \times 10^{27} + 3.6 \times 10^{27} \sim 5 \times 10^{27}$ ergs s^{-1}. The heat flux generated at the slow shock can be estimated from the conduction flux,

$$E_H \sim 2 s_r \kappa_0 T^{7/2}/l , \tag{11}$$

where s_r is the cross-sectional area of the high-temperature ridges (width of the high-temperature ridges times the assumed line-of-sight thickness), and l is the temperature scale length along the high-temperature ridges. The numerical factor 2 comes from the fact that the heat is dumped along both the ridges. The heat flux from the slow shock is $E_H \sim 9 \times 10^{27}$ ergs s^{-1} for $T \sim 12$ MK, $l \sim 6 \times 10^4$ km, and $s_r \sim 4.5 \times 10^{18}$ cm^2 (width of the high-temperature ridges $\sim 9 \times 10^3$ km and the assumed line-of-sight length $= 5 \times 10^4$ km). The ohmic heating at the X-point would not be effective owing to its extremely small geometrical size. The combined energy flux generated by magnetic reconnection is then 1.4×10^{28} ergs s^{-1} and is enough to supply the energy for the flare. The energy that goes to the mass flow may eventually be converted into nonthermal electrons (Tsuneta 1994, 1995) and the heating of the plasma by the perpendicular shock.

The energy produced in the flare (1.4×10^{28} ergs s^{-1}) ultimately has to be supplied by the magnetic fields. Magnetic reconnection serves as an efficient engine to convert the magnetic energy to plasma kinetic and thermal energies. Let us estimate the magnetic energy that is fed to the reconnection site. The magnetic energy supplied to the reconnection site can be written as follows:

$$E_B = \frac{B_{up}^2}{8\pi} SV , \tag{12}$$

where B_{up} is the magnetic field strength in the upstream, S the cross-sectional area of the reconnection site, and V the flow speed in the upstream. If we take $B_{up} \sim 30$ G, $S \sim 3 \times 10^{19}$ cm^2, and $V \sim 56$ km s^{-1}, we obtain $E_B \sim 6 \times 10^{27}$ ergs s^{-1}. Most of the magnetic energy estimated here is converted to plasma kinetic and thermal energies, because the downstream magnetic field strength is much smaller than that of the upstream. Indeed, the magnetic energy that is fed to the reconnection site is close to the energy production rate of 1.4×10^{28} ergs s^{-1} estimated above. $B_{up} \sim 40$ G is needed to completely match the inflow energy flux with the energy production rate by reconnection.

4. SUMMARY AND DISCUSSION

There is no doubt from the *Yohkoh* observations that magnetic reconnection plays a key physical role for at least some flares (Tsuneta et al. 1992). Magnetic reconnection occurs at a neutral sheet or X-type neutral point above the flare loop. The expansion and the structural change of the entire active-region fields observed prior to the flare would be related to the formation of the neutral sheet, although the detailed mechanism for the formation of the neutral sheet is unclear.

This paper presents a consistent picture of the reconnection region and gives the physical parameters of the reconnection site as far as possible. Tables 1 and 2 summarize these parameters obtained in the previous sections. The reconnection (diffusion) point is estimated to be located about 8–18 $\times 10^4$ km above the apparent top of the flare loop (6×10^4 km) from the consideration of the cooling time of the reconnected loops. The high-temperature ridges located around the outer boundary of the flare loops are heated by the standing slow shocks attached to the diffusion point. The shocks would be almost isothermal owing to the good thermal conductivity. The low-density reconnected loops are continually heated by the shocks and are subsequently filled with evaporated plasma. The initial temperature of the reconnection outflow is as hot as 12–13 MK, the same as the observed ridge temperature, and is conductively cooled on its way from the reconnection site to the top of the dense flare loop. This configuration explains the cool plasma in close proximity to the hot ridges as shown in Figure 6. The quantitative estimates on the upstream and downstream particle fluxes, the energy produced by reconnection, and the magnetic energy in the upstream that is fed to the reconnection site all appear to be consistent.

Whether fast-shock heating occurs or not is marginal in this particular flare. It appears that the cool channel does not satisfy the condition for the formation of the fast shock. This is consistent with the observation that there is no hot source around the top of the flare loop, except in the initial phase. On the other hand, the hard X-ray sources above the loop tops observed in several impulsive flares (Masuda et al. 1994) would be due to such shock heating. Although the complex temperature structure in the rise phase does not allow the detailed analysis, and thus is not well understood, the overall picture of the flare established in this paper is considered to be essentially correct in the rise phase as well.

It appears that the system has the quasi–steady state configuration at least after the peak of the flare. An important question is how the system dynamically reaches such structure from an initial configuration. An investigation into whether other flares have such a cooling channel or not may give us information on the dynamical formation of the reconnection point.

As a final remark, we comment on what drives the magnetic reconnection. After the formation of the neutral sheet structure a few minutes to a few tens of minutes prior to the start of the flare, magnetic reconnection (i.e., the flare) starts without an apparent triggering event or mechanism. It appears from the *Yohkoh* observations that there is no clear driving force to activate this magnetic reconnection. This observation supports the so-called spontaneous fast reconnection model (Ugai 1987, 1989, 1992). In the spontaneous model of magnetic reconnection, anomalous resistivity, highly localized at one point of the neutral sheet, triggers the start of magnetic reconnection. Reconnection is then maintained by positive feedback. The fast outflow due to reconnection rarefies the reconnection region, thinning the current channel, thus maintaining the anomalous resistivity at the neutral sheet by reconnection itself. The anomalous resistivity then makes reconnection continue. If this is the case, the observed time (a few to tens of minutes) between the formation of the preflare cusp structure (neutral sheet) and the start of the flare is regarded as the current buildup time for the anomalous resistivity. The spontaneous nature of the magnetic reconnection seen here may be quite different from other reconnection phenomena discovered with *Yohkoh*. For instance, emerging flux interacting with existing coronal fields (Shibata et al. 1994) appears to have the nature of driven reconnection. The buoyant force of the emerging flux acts as the driving force for reconnection to proceed in this case.

This paper demonstrates from the *Yohkoh* observations that magnetic reconnection is responsible for significant energy release of the solar flare. Magnetic reconnection serves as a

highly efficient engine for converting magnetic energy into plasma kinetic and thermal energies with standing slow shocks. This implies an important role for magnetic reconnection for energetic phenomena in other astrophysical as well as magnetospheric contexts.

The author thank S. M. Ugai for his comments on the paper, and T. Yoshida for his help in the scattering correction for Figure 7. The author also would like to thank H. Hudson, L. Acton, and R. Kano for their comments on this paper, and T. Forbes for his encouragement to this work.

REFERENCES

Cargill, P. J., & Priest, E. R. 1983, ApJ, 266, 383
Carmichael, H. 1964, in AAS-NASA Symp. on Solar Flares, ed. W. N. Hess (NASA SP-50), 451
Forbes, T. G., & Malherbe, J. M. 1991, Sol. Phys., 135, 361
Forbes, T. G., & Priest, E. R. 1982, Sol. Phys., 81, 303
———. 1983, Sol. Phys., 84, 169
Hara, H., Tsuneta, S., Acton, L., Bruner, M., Lemen, J., & Ogawara, Y. 1994, PASJ, 46, 493
Hirayama, T. 1974, Sol. Phys., 34, 323
Kano, R., & Tsuneta, S. 1995, ApJ, 454, 934
Kopp, R. A., & Pneuman, G. W. 1976, Sol. Phys., 50, 85
Masuda, S., Kosugi, T., Hara, H., Tsuneta, S., & Ogawara, Y. 1994, Nature, 371, 495
Mewe, R., Gronenschild, E. H. B. M., & van den Oord, G. H. J. 1985, A&AS, 62, 197
Mewe, R., Lemen, J., & van den Oord, G. H. J. 1986, A&AS, 63, 511
Petschek, H. E. 1964, in AAS-NASA Symp. on Solar Flares, ed. W. N. Hess (NASA SP-50), 425
Pneuman, G. W. 1981, in Solar Flare Magnetohydrodynamics, ed. E. R. Priest (New York: Gordon & Breach), 379
Priest, E. R. 1982, Solar, Magnetohydrodynamics (Dordrecht: Reidel)
Shibata, K., Nitta, N., Matsumoto, R., Tajima, T., Yokoyama, T., Hirayama, T., & Hudson, H. S. 1994, in X-Ray Solar Physics from *Yohkoh*, ed. Y. Uchida, H. S. Hudson, T. Watanabe, & K. Shibata (Tokyo: Universal Academy), 29
Sturrock, P. A. 1966, Nature, 211, 695
Tsuneta, S. 1993, in IAU Colloq. 141, The Magnetic and Velocity Fields of Solar Active Regions, ed. H. Zirin, & G. Ai (San Francisco: ASP), 239
———. 1994, in X-Ray Solar Physics from *Yohkoh*, ed. Y. Uchida, H. S. Hudson, T. Watanabe, & K. Shibata (Tokyo: Universal Academy), 115
———. 1995, PASJ, in press
Tsuneta, S., Hara, H., Shimizu, T., Acton, L., Strong, K., Hudson, H., & Ogawara, Y. 1992, PASJ, 44, L63
Ugai, M. 1987, Geophys. Res. Lett., 14, 103
———. 1989, Phys. Fluid B, 1, 942
———. 1992, Phys. Fluids B, 4, 2953
Yoshida, T., & Tsuneta, S. 1996, ApJ, in press